

INLET OPTIMIZATION DESIGN OF A BOUNDARY LAYER INGESTION PROPULSION SYSTEM

Xukang Ma[1], Huicheng Yang[1], Kai You[1], Rongbo Zhu[1], Zhenli Chen[1, 2]

[1]School of Aeronautics, Northwestern Polytechnical University, Xi'an 710072, China
[2]National Key Laboratory of Aircraft Configuration Design, Xi'an 710072, China

Abstract

Boundary Layer Ingestion (BLI) propulsion systems can significantly improve aircraft propulsive efficiency, but severe inlet distortion remains a critical challenge. To address this issue, this work develops an adjoint-based aerodynamic optimization framework for BLI inlet design. A fan body force model (BFM) is incorporated into the optimization process to account for propulsion–airframe coupling effects with substantially reduced computational cost. The proposed methodology is first validated using the IFCPT S-duct benchmark case, achieving reductions of 27.4% in the circumferential distortion index (CDI). Subsequently, the framework is applied to the optimization of a BLI propulsion system integrated into quasi-periodic fuselage of a blended-wing-body-based configuration under the operating condition at Mach number 0.5 and fan rotating speed of 90%. Optimization results show that the optimized inlet effectively suppresses flow separation and secondary-flow structures inside the duct, resulting in a more uniform fan-face flow field. Compared with the baseline configuration, the optimized design achieves approximately 13.4% reduction in the distortion index DC60, approximately 0.5% improvement in total pressure recovery, and significantly reduced swirl distortion at the fan face. Flow-field analysis indicates that the improved aerodynamic performance is primarily associated with the redistribution of adverse pressure gradients and the enhancement of flow attachment throughout the duct. The present study demonstrates that the proposed adjoint-based framework combined with the fan body force model provides an efficient and effective approach for the aerodynamic design and optimization of BLI propulsion system inlets.

Keywords: Boundary layer ingestion; Discrete adjoint method; Inlet optimization; Blended wing body; Body force model

1. Introduction

In response to global climate change and increasingly stringent environmental regulations, the civil aviation industry faces growing pressure to improve fuel efficiency and to reduce emissions. Under these conditions, enhancing propulsion system efficiency has become a central design challenge. While increasing the bypass ratio of turbofan engines has traditionally been an effective approach to improve fuel efficiency, the associated gains diminish at higher bypass ratios due to the resulting weight and drag penalties[1].

In this background, Boundary Layer Ingestion (BLI) propulsion has emerged as a promising aerodynamic–propulsion integration concept[2]. The fundamental idea of BLI is to embed the propulsor within the aft fuselage to ingest the low-momentum boundary layer flow developing over the airframe surface. By re-energizing the wake deficit flow, the propulsion system can reduce the power required to generate equivalent thrust, thereby improving overall propulsive efficiency[3]. BLI configurations have been shown in various studies to reduce fuel consumption[4][5][6]. Consequently, BLI is widely regarded as a potential enabling technology for meeting future requirements on fuel consumption, emissions, and noise reduction proposed in strategic initiatives such as "Flightpath 2050"[7][8].

Meanwhile, increasing attention has also been devoted to advanced aircraft configurations and distributed propulsion concepts[9]. Distributed Fan Propulsion (DFP) systems, which employ multiple ducted fans distributed over the airframe, offer several potential advantages, including high effective bypass ratio, powered-lift enhancement, and improved control effectiveness. More importantly, DFP configurations provide favorable integration opportunities for BLI propulsion systems, enabling enhanced aerodynamic-propulsion coupling and improved overall aircraft efficiency. In addition, DFP

concepts can be effectively combined with Blended Wing Body (BWB) configurations[10]. Compared with conventional configurations, BWB aircraft integrate the fuselage and wing into a unified lifting body, exhibiting higher aerodynamic efficiency.

However, despite their substantial potential benefits, BLI propulsion systems also introduce severe aerodynamic challenges [11]. Continuous ingestion of highly non-uniform boundary layer flow causes the fan blades to operate under strongly distorted inflow conditions, leading to circumferential variations in blade loading and incidence angle. Such distortion may induce local flow separation, deteriorate fan aerodynamic performance, reduce stall margin, increase flutter risk, and ultimately compromise propulsion system stability[12][13]. Therefore, mitigating inlet distortion and improving flow uniformity have become critical issues in the design of BLI propulsion systems.

As a key aerodynamic interface between the airframe and propulsion system, the inlet plays a dominant role in determining the distortion characteristics at the fan-face. An appropriately designed BLI inlet must simultaneously achieve high total pressure recovery, low distortion intensity, and favorable boundary layer ingestion capability under strong aerodynamic coupling conditions. However, many existing studies simplify the propulsion system by neglecting fan effects during inlet design and optimization. Although such treatments reduce computational cost, they cannot accurately capture the coupled aerodynamic interaction between the inlet flow and the propulsion system, potentially leading to discrepancies between the optimized flow field and the actual operating conditions. Conversely, high-fidelity approaches that explicitly model the propulsion system can significantly improve the realism of distortion prediction, but introduce prohibitively high computational costs, particularly for optimization processes. In addition, surrogate-model-based optimization methods commonly employed in aerodynamic design generally require a large number of high-fidelity sample evaluations to construct the design space, which further increases the computational burden for complex BLI configurations involving highly three-dimensional separated flows and propulsion–airframe coupling effects. Therefore, developing a computationally efficient optimization framework capable of retaining the essential propulsion–flow interaction physics remains an important research challenge.

To address these issues, this work develops an adjoint-based optimization framework for the aerodynamic design of a BLI propulsion system inlet. A previously validated fan body force model (BFM) is incorporated into the optimization process to represent the fan aerodynamic effects with substantially reduced computational cost while preserving the primary distortion-related flow physics. Compared with conventional approaches, the adjoint method enables efficient high-dimensional shape optimization with significantly improved computational efficiency. First, the employed optimization methodology is validated using the IFCPT S-duct benchmark configuration. Subsequently, the proposed framework is applied to the optimization design of a representative BLI propulsion system inlet, including the configuration description, optimization process, and detailed analysis of flow-field evolution.

2. Optimization Methodology

2.1 Discrete Adjoint Formulation

Adjoint methods for aerodynamic shape optimization can be categorized into continuous and discrete approaches according to the order of differentiation and discretization. The continuous adjoint method adopts a differentiate-then-discretize strategy, which preserves clear physical interpretations. However, truncation errors may introduce inconsistencies between the computed gradients and the discrete flow solution. In addition, analytical derivation becomes increasingly difficult for complex turbulence models. In contrast, the discrete adjoint method is derived directly from the discretized governing equations. Although this approach generally requires higher memory consumption, it provides gradients that are fully consistent with the numerical discretization scheme. Consequently, the discrete adjoint method has become the standard approach in most commercial Computational Fluid Dynamics (CFD) solvers.

The discrete adjoint formulation is based on the residual form of the Navier–Stokes equations and the objective function[14], which can be written as

$$\boldsymbol{R}(\boldsymbol{x}, \boldsymbol{w}) = 0 \tag{1}$$

$$J = J(\boldsymbol{x}, \boldsymbol{w}) \tag{2}$$

Where $\boldsymbol{x}$ represents the geometric design variable vector, $\boldsymbol{w}$ denotes the flow field variables, $\boldsymbol{R}$ is the residual vector of the discretized governing equations, and J is the objective function. When the body-force model is included, the residual vector additionally contains source-term contributions.

Applying the chain rule, the total derivative of the objective function with respect to the design variables is expressed as:

$$\frac{dJ}{d\boldsymbol{x}} = \frac{\partial J}{\partial \boldsymbol{x}} + \frac{\partial J}{\partial \boldsymbol{w}} \frac{d\boldsymbol{w}}{d\boldsymbol{x}} \tag{3}$$

The flow-field derivative can be obtained by differentiating the residual equations:

$$\frac{d\boldsymbol{R}}{d\boldsymbol{x}} = \frac{\partial \boldsymbol{R}}{\partial \boldsymbol{x}} + \frac{\partial \boldsymbol{R}}{\partial \boldsymbol{w}} \frac{d\boldsymbol{w}}{d\boldsymbol{x}} = 0 \tag{4}$$

$$\frac{d\boldsymbol{w}}{d\boldsymbol{x}} = -\left[\frac{\partial \boldsymbol{R}}{\partial \boldsymbol{w}}\right]^{-1} \frac{\partial \boldsymbol{R}}{\partial \boldsymbol{x}} \tag{5}$$

Direct evaluation of $d\boldsymbol{w}/d\boldsymbol{x}$ requires inversion of the Jacobian matrix, which is computationally expensive. To avoid this operation, the adjoint variable $\boldsymbol{\psi}$ (Lagrange multiplier vector) is introduced to construct the augmented Lagrangian function L:

$$L = J - \boldsymbol{\psi}^T \boldsymbol{R} \tag{6}$$

Since $\boldsymbol{R} = 0$, the total derivative can be rewritten as:

$$\frac{dJ}{d\boldsymbol{x}} = \frac{\partial J}{\partial \boldsymbol{x}} - \boldsymbol{\psi}^T \frac{\partial \boldsymbol{R}}{\partial \boldsymbol{x}} + \left(\frac{\partial J}{\partial \boldsymbol{w}} - \boldsymbol{\psi}^T \frac{\partial \boldsymbol{R}}{\partial \boldsymbol{w}}\right) \frac{d\boldsymbol{w}}{d\boldsymbol{x}} \tag{7}$$

Taking the derivative of the augmented Lagrangian with respect to the flow variables and setting it to zero yields the discrete adjoint equation:

$$\left[\frac{\partial \boldsymbol{R}}{\partial \boldsymbol{w}}\right]^T \boldsymbol{\psi} = \left[\frac{\partial J}{\partial \boldsymbol{w}}\right]^T \tag{8}$$

Solving Eq. (8) yields the adjoint variables, which are subsequently used to evaluate the sensitivity of the objective function with respect to the design variables.

2.2 Gradient-Based Optimization Algorithm

The sensitivities obtained from the discrete adjoint equations are used to update the geometry toward improved aerodynamic performance. In this work, the steepest descent method is adopted for gradient-based optimization[15]. The procedure consists of three components: search direction determination, step-size control, and sensitivity smoothing.

In the design space, the objective function is minimized along the negative gradient direction. Let $\boldsymbol{x}_n$ denote the design variable vector and $\nabla J(\boldsymbol{x}_n)$ represent the corresponding gradient vector. The iterative update scheme is expressed as

$$\delta \boldsymbol{x}_n = -\lambda_n \nabla J(\boldsymbol{x}_n) \tag{9}$$

$$\boldsymbol{x}_{n+1} = \boldsymbol{x}_n + \delta(\boldsymbol{x}_n) \tag{10}$$

Where λ_n is the step size, the negative sign indicates searching along the negative gradient direction for minimization (positive for maximization), and $\delta(\boldsymbol{x}_n)$ is the design variable update proportional to local sensitivity. Regions with larger sensitivity magnitudes undergo greater geometric deformation during the optimization process.

The step size strongly affects optimization stability and convergence efficiency. Since the adjoint sensitivities only represent local linear behavior, excessively large step sizes may lead to oscillatory convergence or mesh distortion, whereas excessively small values slow down convergence. Therefore,

a deformation-limiting strategy is employed in the present study. By prescribing the maximum allowable geometric displacement, the scaling factor for each iteration is automatically determined to maintain mesh quality and ensure robust convergence.

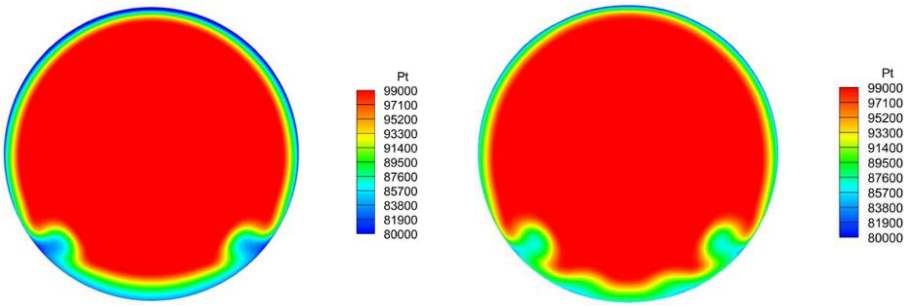
2.3 Method Validation

The IFCPT S-duct inlet from Section PAW-4[16] is selected to validate the discrete adjoint optimization method. Kamat et al.[17] previously performed adjoint optimization on the same configuration. The present study adopts the same objective function, aimed at minimizing flow distortion at the fan-face plane:

$$J = \frac{\sum_f |A_f| \left(P_{t,f} - \bar{P}_{t,f} \right)^2}{\sum_f |A_f|} \tag{11}$$

where f denotes a grid cell face, A_f is the cell face area, $P_{t,f}$ represents the total pressure on the face, and $\bar{P}_{t,f}$ is the area-averaged total pressure at the outlet plane.

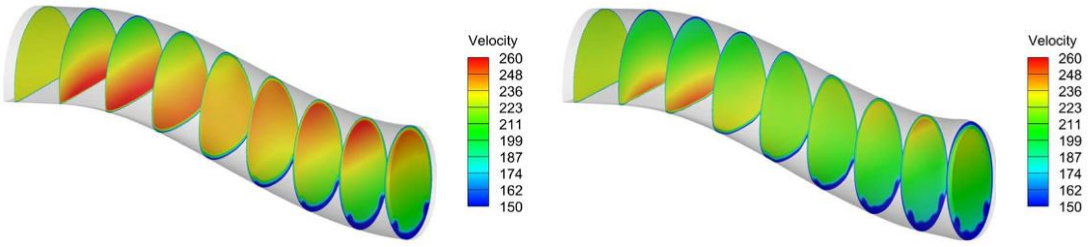
The total pressure distributions at the fan-face plane for the baseline and optimized configurations are shown in Fig. 1. In the baseline case, a low total pressure core forms near the lower wall, dominated by a pair of counter-rotating vortices. After optimization, the low-pressure region at the bottom persists but exhibits reduced peak magnitude. The low-pressure region near the top wall is diminished, resulting in a more uniform total pressure distribution.



(a) Baseline configuration (b) Optimized configuration

Fig. 1 Total pressure distributions of IFCPT S-duct at fan-face plane before and after optimization

The velocity distributions along streamwise sections for both configurations are shown in Fig. 2. In the baseline configuration, a high-velocity region develops near the lower wall after the first bend and shifts toward the upper wall in the second bend due to wall curvature. Optimization suppresses local acceleration: the peak velocity and spatial extent at the first bend are reduced, and the high-velocity region in the second bend is mitigated. Consequently, the streamwise velocity distribution becomes more uniform, which reduces flow losses and improves outlet flow quality. The streamwise section profile comparison is shown in Fig. 3.



(a) Baseline configuration (b) Optimized configuration

Fig. 2 Velocity distributions of IFCPT S-duct along streamwise sections before and after optimization

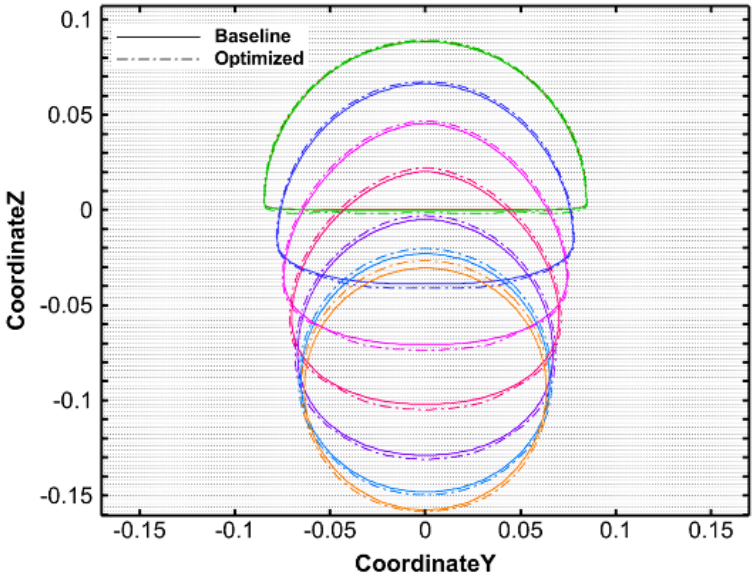


Fig. 3 Streamwise sectional profiles of the IFCPT S-duct before and after optimization

Quantitative assessment is summarized in Table 1. The objective function decreases from 2.4×10^7 (baseline) to 1.5×10^7 (optimized), corresponding to a 35.4% reduction. The circumferential distortion index (CDI) decreases from 0.18 to 0.13, a 27.4% reduction. CDI is defined as shown in Eq. (12). A total pressure rake on the Aerodynamic Interface Plane (AIP) comprising an array of 8 spokes with 5 probes each is shown in Fig. 4. These results demonstrate that the adjoint optimization effectively improves flow uniformity and reduces circumferential distortion, confirming the validity of the method for subsequent inlet optimization applications.

$$\mathrm{CDI}=\underset{i=1}{\overset{n_{\mathrm{radius}}-1}{\mathrm{Max}}}\left(0.5\left[\frac{p_{o,i}-p_{0,\min_i}}{p_{o,\mathrm{avg}}}+\frac{p_{o,i+1}-p_{o,\min_{i+1}}}{p_{o,\mathrm{avg}}}\right]\right) \tag{12}$$

Where $p_{o,\mathrm{avg}}$ is the average total pressure, $p_{o,i}$ denotes the average total pressure of the pressure distribution of the i-th ring and $p_{0,\min}$ represents the minimal pressure of the i-th ring.

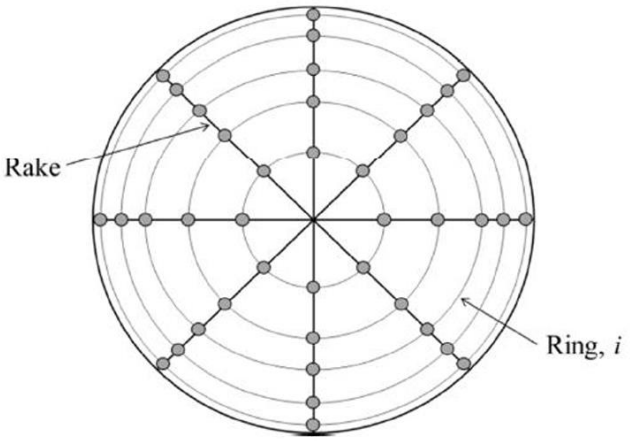


Fig. 4 8×5 rake and ring AIP discretization for inlet flow distortion measurements

Table 1 Aerodynamic performance comparison of IFCPT S-duct inlet before and after optimization

Configuration	Objective Function Value/(Pa²)	Change in Objective/(%)	CDI	Change in CDI/(%)
Baseline	2.4×10^7	-	0.18	-
Optimized	1.5×10^7	-35.4	0.13	-27.4

3. Optimization Results and Flow Analysis

3.1 Problem Formulation and Optimization Framework

The BLI configuration investigated in this work is shown in Fig. 5. It comprises a quasi-two-dimensional airframe based on a BWB symmetry-plane profile, with an embedded propulsion system unit integrated into the aft fuselage. The propulsion system is modeled using a body-force approach, where the fan work is simulated through source terms in the momentum and energy equations. Detailed methodology and validation of this model will be reported in a forthcoming publication.

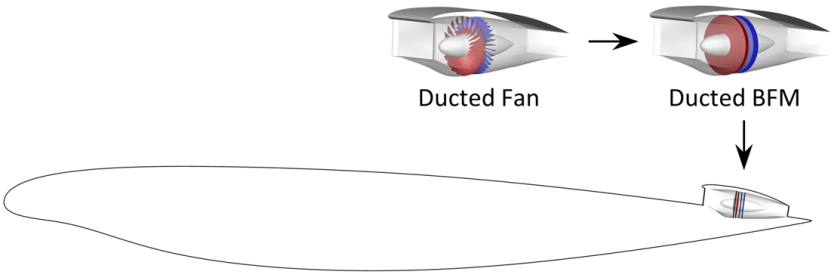


Fig. 5 Quasi-two-dimensional BLI propulsion system with an embedded fan

A well-defined optimization framework is adopted to achieve optimal trade-offs in inlet aerodynamic performance under complex boundary constraints. The core objectives for turbofan engine inlet design are: (1) maximize the total pressure recovery coefficient at the fan-face plane, and (2) minimize total pressure distortion under the specified flight conditions. These objectives aim to improve flow uniformity at the fan-face and reduce stall and flutter risks induced by flow separation. The present study employs a gradient-based optimization framework using discrete adjoint methods. The optimization strategy can be summarized as:

$$\begin{aligned} &Objectives: && \min \begin{bmatrix} -PR \\ DC_{60} \end{bmatrix} \\ &\text{Constraints}: && A_{th} = A_{th}^{ref}, A_f = A_f^{ref} \\ & && \boldsymbol{S} \in C^2 \\ & && \boldsymbol{z}_{left} = -\boldsymbol{z}_{right} \end{aligned} \tag{13}$$

where PR is pressure recovery coefficient, A_{th} represents the diffuser section area, A_f denotes fan-face area, A_{th}^{ref} and A_f^{ref} are the inlet and outlet areas of the baseline configuration, $\boldsymbol{S}$ represents the geometric surface, and $\boldsymbol{z}$ is the coordinate vector of geometric surface control points in the z-direction. Geometric parameterization and mesh deformation are achieved through a RBF-based dynamic mesh method, which smoothly propagates wall displacement fields to internal grid nodes, enabling continuous and controllable shape deformation while maintaining mesh quality. Gradient information of the objective function with respect to design variables is obtained by solving discrete adjoint equations. Iterative optimization is performed using the steepest descent method, cycling through flow-field solution, adjoint solution, gradient update, and mesh deformation until convergence of the objective function.

3.2 Design Sensitivity Analysis

During the initial optimization iteration, gradient information is used to identify geometric regions with significant impact on aerodynamic performance. Fig. 6 shows the Shape Sensitivity distribution (SS) at Mach number 0.5 and fan rotating speed of 90%. High sensitivities are observed at the inlet, corner regions, and sidewalls, corresponding to areas with strong curvature variations that are prone to secondary flows and flow separation. Small geometric perturbations in these regions can induce significant changes in downstream flow topology. The Normal Optimal Displacement (NOD) is shown in Fig. 7. The lower wall exhibits inward contraction (positive displacement), whereas the upper wall and fan leading-edge region exhibit outward expansion (negative displacement). These sensitivity

trends indicate the regions where geometric modifications will most effectively influence aerodynamic performance.

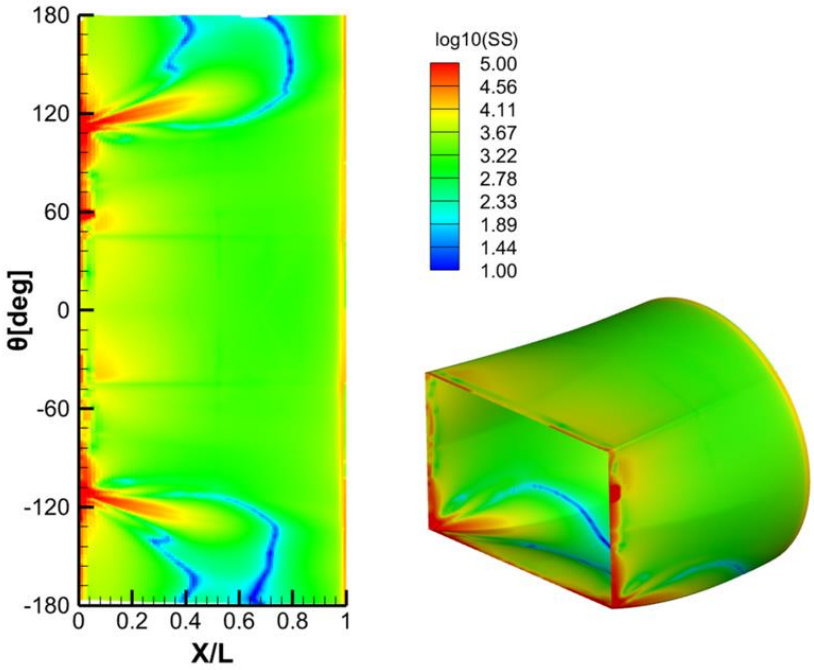


Fig. 6 Shape sensitivity distribution on inlet surface at M=0.5 and Ω=90%.

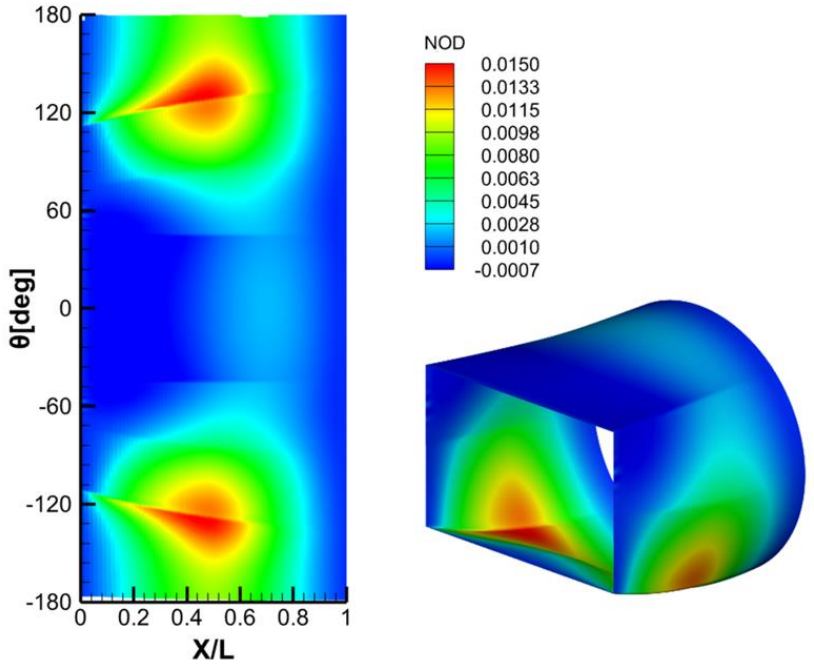
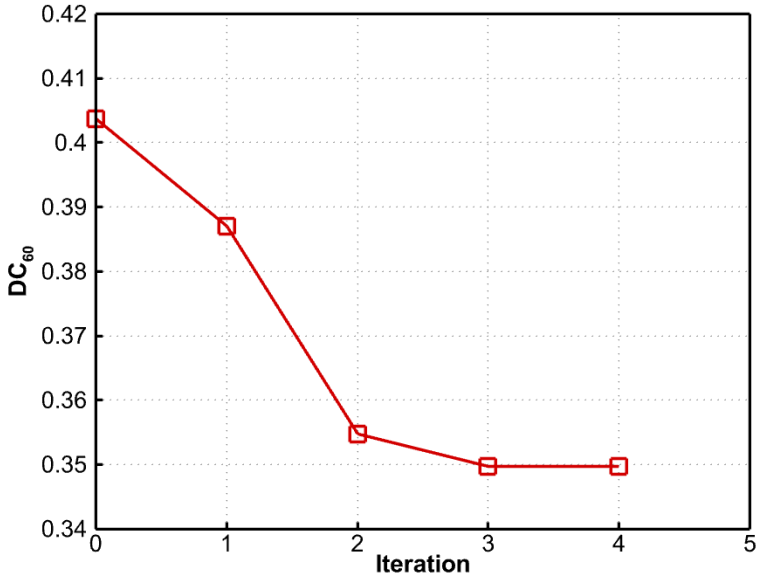


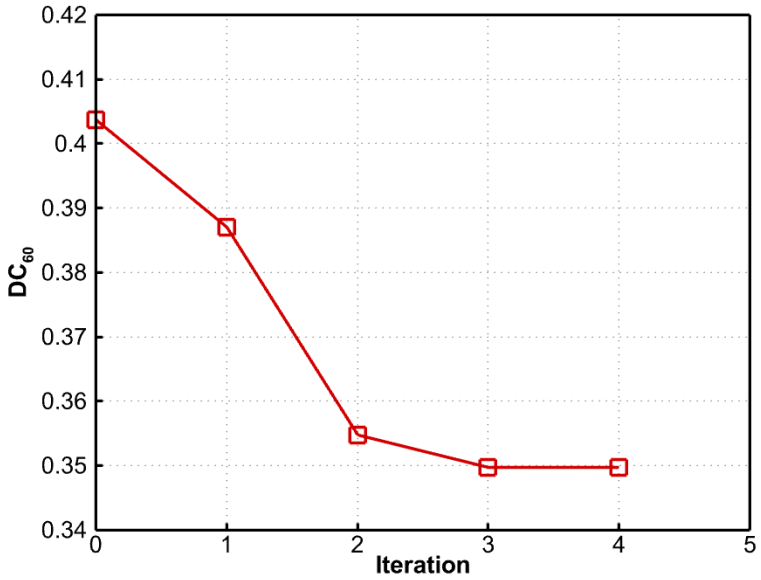
Fig. 7 Normal displacement distribution on inlet surface at M=0.5 and Ω=90%.

3.3 Convergence History and Performance Metrics

The optimization converges after four design cycles. Fig. 8 presents the evolution of the inlet total pressure recovery coefficient and distortion index during the optimization process. As the iterations proceed, the total pressure recovery coefficient increases monotonically, whereas the distortion index decreases continuously, indicating progressive improvement in inlet aerodynamic performance and fan-face flow uniformity.



(a) Inlet total pressure recovery



(b) Inlet distortion index

Fig. 8 Inlet performance evolution during optimization at M=0.5 and Ω=90%.

3.4 Geometric Deformation Characteristics

The wall profiles and streamwise section shapes between the baseline and optimized configurations are shown in Fig. 9 and Fig. 10. The inlet adopts an asymmetric diffuser geometry with a nearly flat upper wall and an S-shaped lower wall. Geometric deformation in the optimized configuration is concentrated primarily on the lower wall and corner regions, consistent with the high-sensitivity regions identified in the adjoint sensitivity analysis. The streamwise profile comparison shows that, in the front portion of the duct (approximately 0–40%L), the optimized configuration reduces local curvature variation and decreases the cross-sectional area growth rate. This modification alleviates the local diffusion burden in the upstream region. In the downstream portion, the wall curvature and area distribution are redistributed, with the lower wall shifting upward relative to the baseline configuration. Cross-sectional comparisons indicate that geometric changes on the upper wall are relatively minor, whereas deformation is concentrated near the lower wall and corner regions. At the 20%L section, the corner region contracts toward the flow passage. Between the 40%L and 60%L sections, the lower wall exhibits more pronounced inward contraction, producing significant profile changes. Near the 80%L section, the deformation gradually weakens to satisfy the outlet geometric constraint. Overall,

the optimization reconstructs the wall curvature and cross-sectional area distribution to alleviate adverse pressure gradients and suppress secondary-flow development.

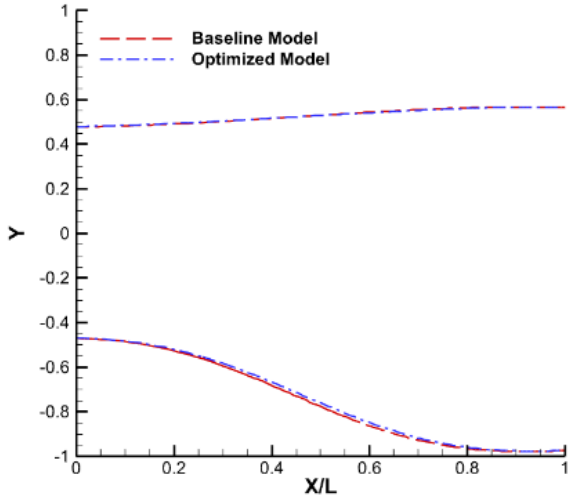
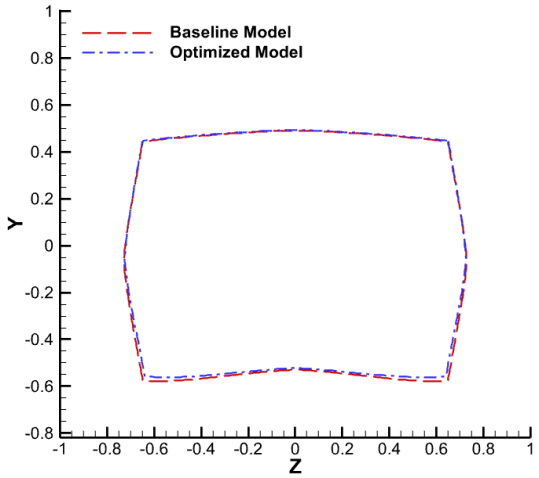
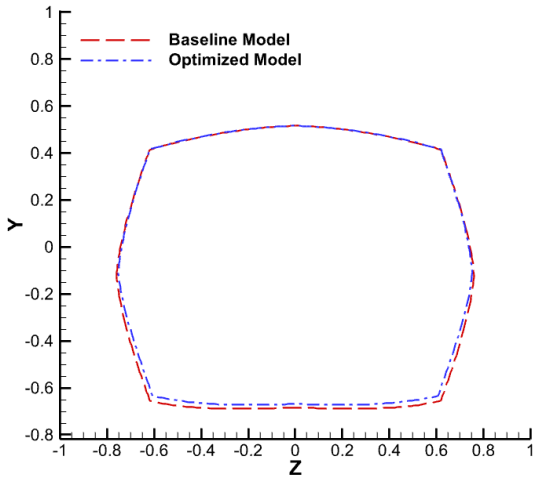


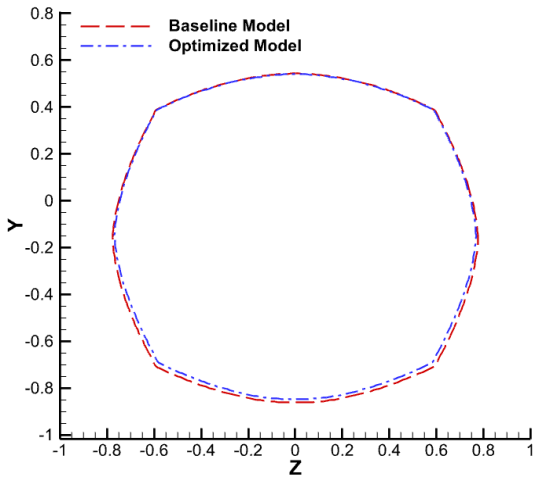
Fig. 9 Upper/lower wall profiles at M=0.5 and Ω=90%.



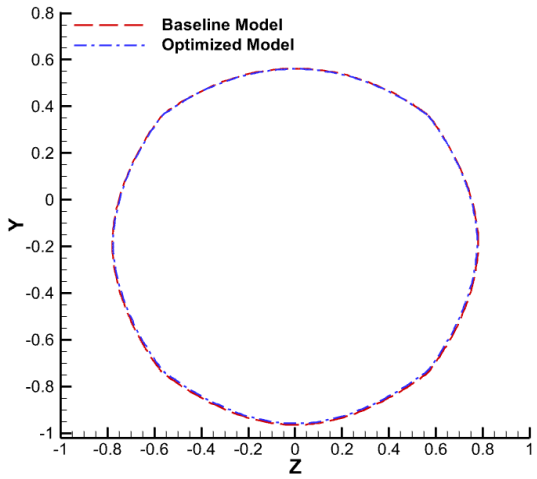
(a) 20%L section



(b) 40%L section



(a) 60%L section



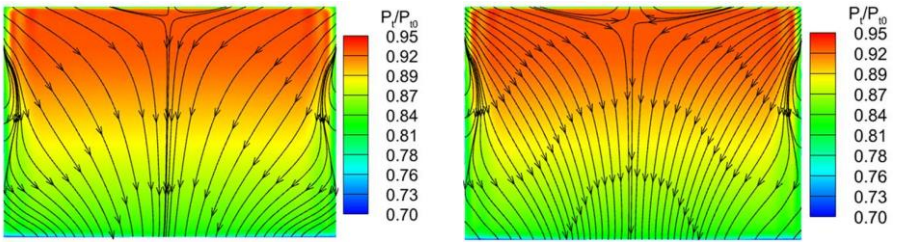
(b) 80%L section

Fig. 10 Wall profiles along streamwise sections at M=0.5 and Ω=90%.

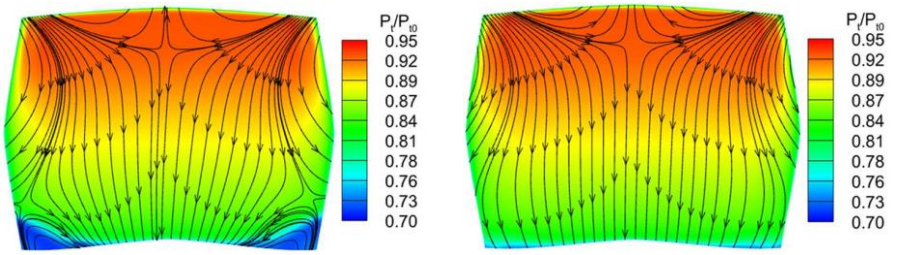
3.5 Flow Field and Aerodynamic Performance

The total pressure distributions along streamwise sections for both configurations are shown in Fig.

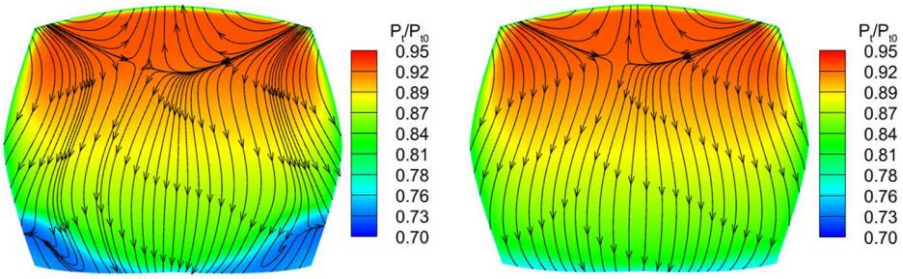
11. At the inlet entrance, both configurations exhibit nearly identical total pressure distributions, indicating consistent inflow conditions. At the 20%L section, the baseline configuration exhibits a pronounced low-total-pressure region near the corner, indicating early development of local losses and distortion. In the optimized configuration, both the extent and intensity of this low-pressure region are reduced, indicating suppression of loss generation in the upstream region. Minimal differences are observed in the upper flow region, consistent with the relatively small geometric deformation in this area. At the 40%L section, the corner low-pressure region in the baseline configuration expands further, accompanied by increased distortion intensity. In contrast, the optimized configuration suppresses the downstream growth of the low-pressure region. At the 60%L and 80%L sections, the baseline configuration continues to exhibit pronounced low-pressure structures, whereas the optimized configuration maintains reduced low-pressure intensity and smaller affected regions. These results indicate that the optimized geometry suppresses the streamwise growth of low-momentum flow and improves overall flow uniformity.



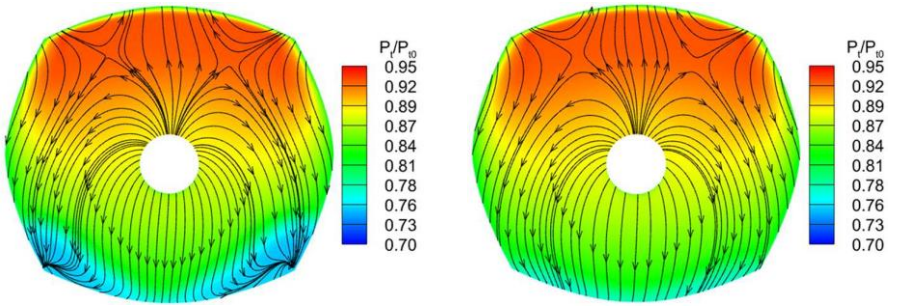
(a) Inlet entrance section



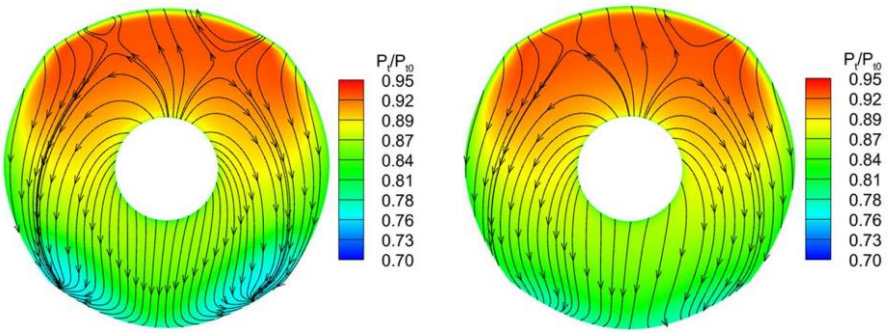
(b) 20%L section



(c) 40%L section



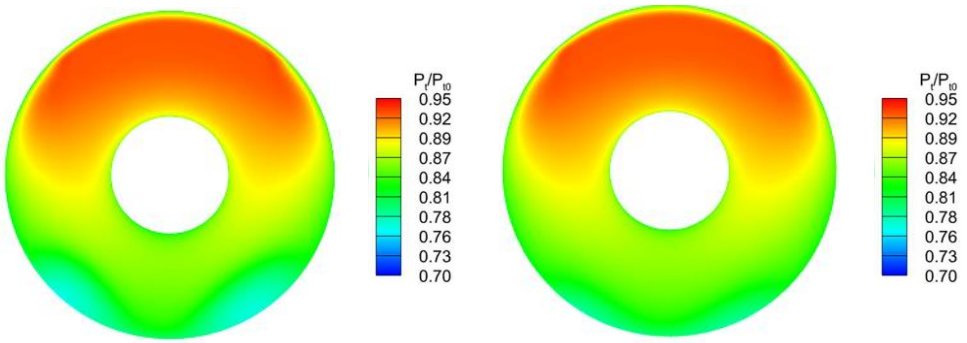
(d) 60%L section



(e) 80%L section

Fig. 11 Total pressure distributions along streamwise sections at M=0.5 and Ω=90%.

The total pressure distributions on the AIP are shown in Fig. 12. The baseline configuration exhibits two concentrated low-total-pressure regions near the corner sectors, producing strong distortion at the fan-face. In contrast, the optimized configuration exhibits a substantially more uniform total pressure distribution, with the concentrated low-pressure regions largely eliminated. Quantitative performance comparisons are summarized in Table 2. The inlet total pressure recovery coefficient increases from 0.986 to 0.991, corresponding to an improvement of approximately 0.5%. Meanwhile, DC60 decreases from 0.40 to 0.35, representing a reduction of approximately 13.4%. These results confirm that the optimized configuration improves inlet flow quality and reduces circumferential distortion at the fan-face.



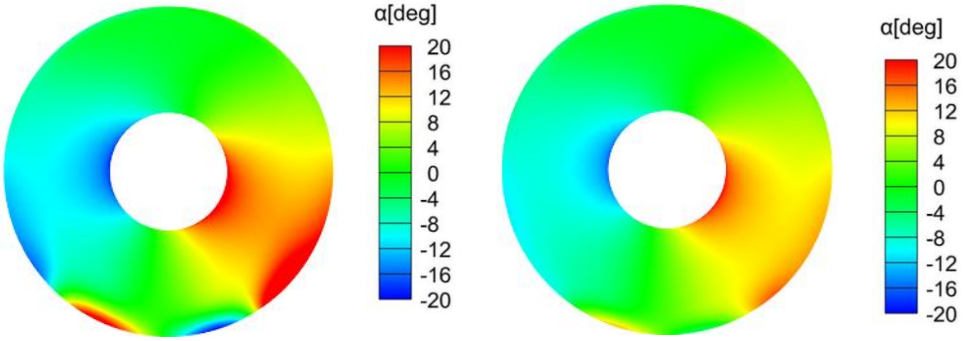
(a) Baseline configuration (b) Optimized configuration

Fig. 12 Total pressure distributions on AIP at M=0.5 and Ω=90%.

Table 2 Inlet performance parameters at M=0.5 and Ω=90%.

Parameter	Baseline	Optimized	Change/(%)
PR	0.986	0.991	0.5
DC60	0.40	0.35	-13.4

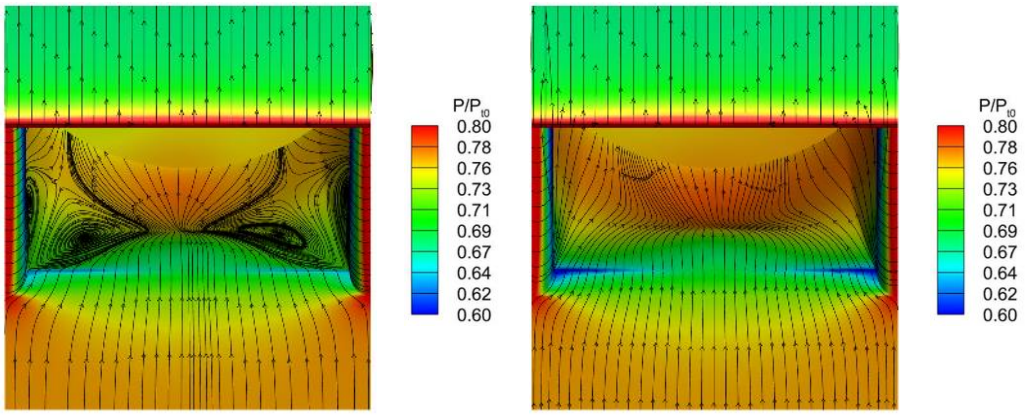
The distorted flow region induces circumferentially non-uniform static pressure upstream of the fan, causing surrounding flow to converge toward the low-pressure region. As a result, circumferential variations in swirl angle develop through the duct. Fig. 13 presents the circumferential distribution of absolute swirl angle at the fan-face mid-span. When the rotor enters the distortion sector, the incoming flow exhibits co-rotating swirl characteristics, corresponding to positive swirl-angle peaks. In this region, the incoming swirl direction aligns with rotor rotation, reducing blade incidence angle and delaying flow separation, although blade loading is correspondingly weakened. Conversely, when the rotor exits the distortion sector, the flow exhibits counter-rotating characteristics with negative swirl-angle peaks. The opposing swirl direction increases blade incidence angle, which may enhance blade loading but also increases the risk of local separation and unsteady aerodynamic loading. The baseline configuration exhibits larger swirl-angle peaks than the optimized configuration, indicating stronger swirl distortion at the AIP. The optimized configuration therefore reduces the likelihood of local fan-flow separation.



(a) Baseline configuration (b) Optimized configuration

Fig. 13 Absolute swirl angle distributions on AIP at M=0.5 and Ω=90%.

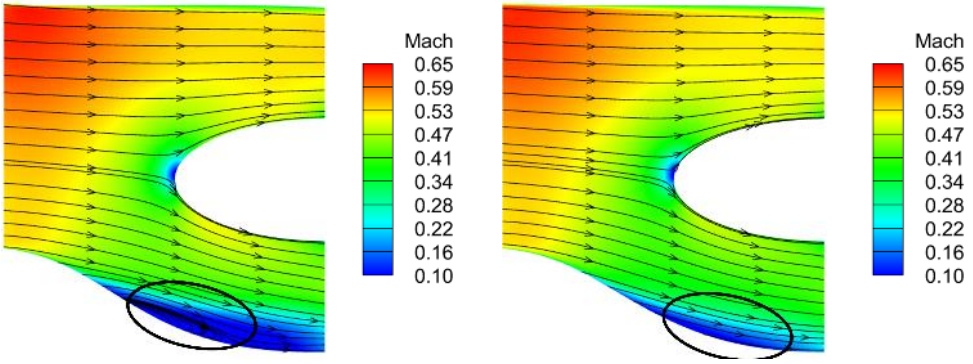
The wall streamlines of the two configurations are shown in Fig. 14. In the baseline configuration, the lower-wall corner region exhibits clear vortical structures, indicating strong corner separation and recirculation. Streamlines on the lower surface first converge toward the symmetry plane and then diverge downstream of the recirculation region, demonstrating strong secondary-flow effects in the near-wall region. In the optimized configuration, the streamlines become more uniformly aligned with the streamwise direction, and the vortical structures disappear. This indicates suppression of flow separation and weakened secondary-flow intensity, which contributes to reducing low-total-pressure-region formation at the duct outlet.



(a) Baseline configuration (b) Optimized configuration

Fig. 14 Wall static pressure and surface streamline distributions at M=0.5 and Ω=90%.

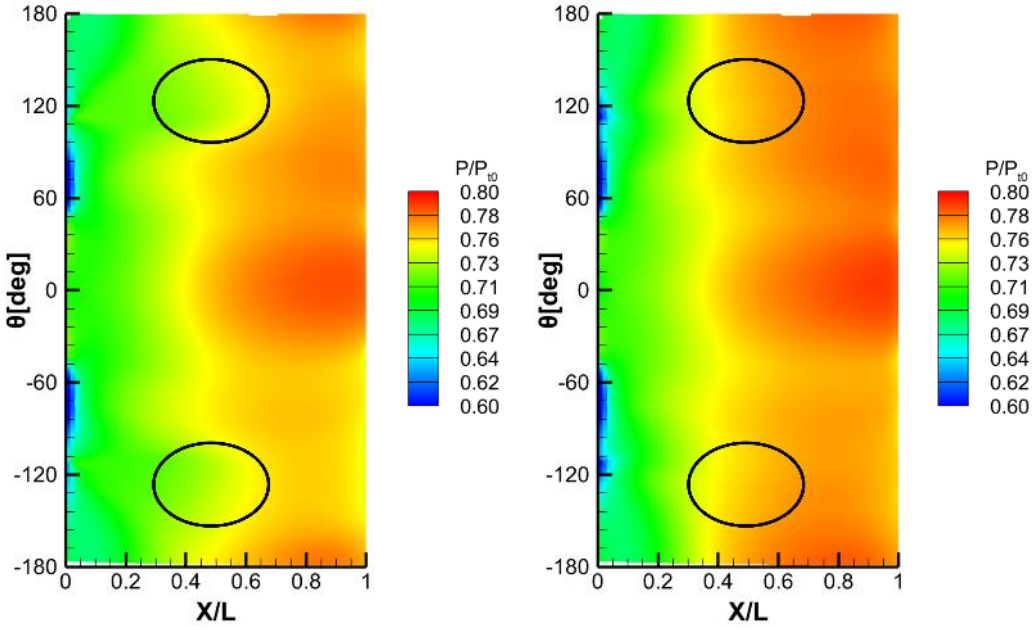
Mach number distributions at the θ=120° azimuthal section are shown in Fig. 15. In the baseline configuration, a large low-velocity region forms near the corner region, accompanied by substantial boundary-layer thickening and local recirculation. These features indicate strong adverse pressure gradients that induce flow separation and significant total pressure loss. In contrast, the optimized configuration substantially reduces the low-velocity region. The near-wall flow remains attached throughout the duct, and no evident recirculation structure is observed. These results demonstrate that the optimized geometry alleviates adverse pressure gradients and enhances boundary-layer resistance to separation.



(a) Baseline configuration (b) Optimized configuration

Fig. 15 Mach number and apatial streamline distributions at θ=120° section, M=0.5 and Ω=90%.

Inlet wall static pressure distributions in unwrapped view are shown in Fig. 16. In the baseline configuration, the highlighted region corresponds to a low-pressure zone associated with local flow acceleration followed by strong adverse pressure gradients. The optimized configuration exhibits a more uniform pressure distribution with increased static pressure levels in this region.



(a) Baseline configuration (b) Optimized configuration

Fig. 16 Unwrapped wall static pressure distributions at M=0.5 and Ω=90%.

Inlet wall static pressure distribution extracted at the azimuthal location of minimum total pressure are shown in Fig. 17. In the baseline configuration, the wall static pressure rises rapidly over a short streamwise distance, indicating a strong adverse pressure gradient that triggers flow separation. The subsequent stagnation in pressure recovery suggests the presence of a separation bubble that inhibits further diffusion. In the optimized configuration, redistribution of wall curvature and cross-sectional area produces a more gradual pressure rise in the upstream region, thereby weakening the local adverse pressure gradient. Consequently, the downstream flow retains greater resistance to separation, and the static pressure recovery process becomes smoother and more continuous along the streamwise direction. This enables fully attached flow throughout the duct, resulting in higher total pressure recovery and lower distortion levels.

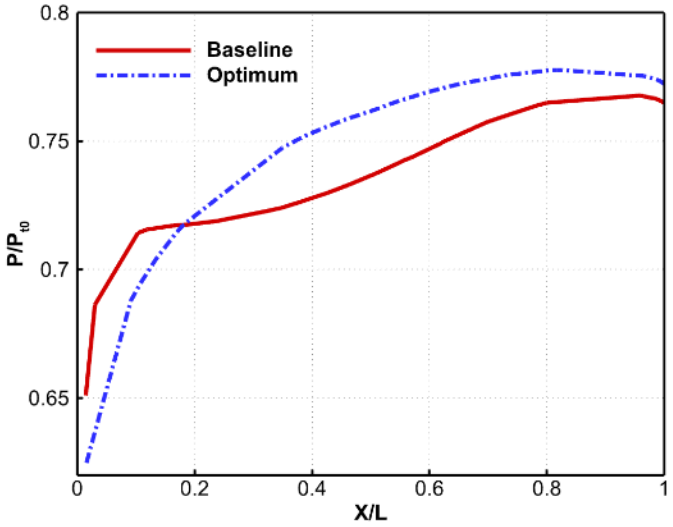


Fig. 17 Wall static pressure distributions at θ=120° at M=0.5 and Ω=90%.

4. Conclusions

This study presents an adjoint-based aerodynamic optimization framework for inlets in boundary layer ingestion propulsion systems and demonstrates its effectiveness through application to a simplified representative BLI configuration. The main conclusions are as follows:

（1） A discrete adjoint methodology combined with RBF-based dynamic mesh and gradient-based iterative optimization enables efficient aerodynamic shape design of complex inlets. Validation using the IFCPT S-duct case confirms significant reductions in the circumferential distortion index by approximately 27.4%, demonstrating the framework's feasibility and computational efficiency.

（2） Application to a BLI inlet integrated with a quasi-two-dimensional BWB airframe and fan body force model results in marked aerodynamic improvements. Optimization reduces the distortion index by approximately 13.4% and swirl intensity at the fan interface while slightly increasing total pressure recovery by approximately 0.5%, showing that targeted geometric adjustments in the lower wall and corner regions effectively mitigate adverse pressure gradients and flow separation.

（3） Analysis of the optimized flow reveals that controlling wall curvature and cross-sectional area growth rates stabilizes streamwise flow, suppresses secondary vortices, and maintains attached flow throughout the duct. These changes enhance the uniformity and quality of the fan-face inflow.

Overall, the framework offers a practical tool for improving BLI inlet performance and may provide guidance for future integrated aircraft concepts incorporating BWB and distributed propulsion configurations.

5. Contact Author Email Address

Corresponding author: zhenlichen@nwpu.edu.cn

6. Copyright Statement

The authors confirm that they, and/or their company or organization, hold copyright on all of the original material included in the paper. The authors also confirm that they have obtained permission, from the copyright holder of any third party material included in the paper, to publish it as part of their paper. The authors confirm that they give permission, or have obtained permission from the copyright holder of the paper, for the publication and distribution of the paper as part of the ICAS proceedings or as individual off-prints from the proceedings.

References

[1] Acar H, Arnson M and Tsai M. Historical trends and future projections of key performance parameters in aircraft design. Journal of Aircraft, pp 1-23, 2025.

[2] Moirou N G M, Sanders D S and Laskaridis P. Advancements and prospects of boundary layer ingestion propulsion concepts. Prog. Aerosp. Sci., Vol. 138, pp 100897, 2023.

[3] Smith L H Jr. Wake ingestion propulsion benefit. Journal of Propulsion and Power, Vol. 9, No. 1, pp 74-82, 1993.

[4] Uranga A, Drela M, Greitzer E M, Hall D K, Titchener N A, Lieu M K, Siu N M, Huang A C, Gatlin G M and Hannon J A. Boundary layer ingestion benefit of the D8 transport aircraft. AIAA Journal, Vol. 55, No. 11, pp 3693-3708, 2017.

[5] Welstead J and Felder J L. Overview of the NASA STARC-ABL (Rev. B) advanced concept. NASA/TM-2017-219663, March 2017.

[6] Roberts T W, Eastbourn S, Zhao X and Dowdle A. Comparison of blended wing body and tube-and-wing performance for regional aircraft. The Aeronautical Journal, Vol. 129, No. 1323, pp 148-169, 2025.

[7] European Commission. Flightpath 2050 Europe's Vision for Aviation. Brussels: European Commission, 2011.

[8] National Aeronautics and Space Administration. NASA Aeronautics Strategic Implementation Plan. Washington, DC: NASA, 2017.

[9] Advisory Council for Aviation Research and Innovation in Europe. Delivering Europe's Vision for Aviation, Strategic Research and Innovation Agenda, Volume 1. 2017.

[10] Chen Z L, Zhang M H and Chen Y C. Assessment on critical technologies for conceptual design of blended-wing-body civil aircraft. Chinese Journal of Aeronautics, Vol. 32, No. 8, pp 97-1827, 2019.

[11] Ma T, Lu H and Li Q S. A systematic review of boundary layer ingestion (BLI) fan: Current status and future perspectives. Progress in Aerospace Sciences, 2024.

[12] Florea R V, Matalanis C, Hardin L W, Stucky M and Shabbir A. Parametric analysis and design for embedded engine inlets. J. Propuls. Power, Vol. 31, No. 3, pp 843-850, 2015.

[13] Kurzke J. Effects of inlet flow distortion on the performance of aircraft gas turbines. Journal of Gas Turbines and Power, Vol. 130, No. 4, Paper 041201, 2008.

[14] Kaya H and Tuncer I H. Discrete adjoint-based aerodynamic shape optimization framework for natural laminar flows. AIAA Journal, Vol. 60, No. 1, pp 197-212, 2022.

[15] Jameson A. Aerodynamic shape optimization using the adjoint method. Brussels: Von Karman Institute for Fluid Dynamics, 2003.

[16] Potturi A S, Bhatia A and Oberoi R. Computational analysis of the IFCPT S-Duct using CFD++ for the 4th Propulsion Aerodynamics Workshop. Reston, VA: American Institute of Aeronautics and Astronautics, 2019.

[17] Kamat V, Rao V and Xu M. Flow distortion based S-Duct optimization using adjoint methodology. Reston, VA: American Institute of Aeronautics and Astronautics, 2020.